中国光学（中英文） Chinese Optics 核心期刊

基于互补集合经验模态分解结合希尔伯特变换的光频扫描干涉信号相位提取方法

杨克元 邓忠文 陈文军 姚鑫 孙海峰 沈利荣

Phase-extracting method of optical frequency scanning interference signals based on the CEEMD-HT algorithm

YANG Ke-yuan, DENG Zhong-wen, CHEN Wen-jun, YAO Xin, SUN Hai-feng, SHEN Li-rong

引用本文:
杨克元, 邓忠文, 陈文军, 姚鑫, 孙海峰, 沈利荣. 基于互补集合经验模态分解结合希尔伯特变换的光频扫描干涉信号相位提取方法[J]. 中国光学, 2023, 16(3): 682–700. doi: 10.37188/CO.2022–0173
YANG Ke-yuan, DENG Zhong-wen, CHEN Wen-jun, YAO Xin, SUN Hai-feng, SHEN Li-rong. Phase-extracting method of optical frequency scanning interference signals based on the CEEMD-HT algorithm[J]. *Chinese Optics*, 2023, 16(3): 682-700. doi: 10.37188/CO.2022-0173

在线阅读 View online: https://doi.org/10.37188/CO.2022–0173

文章编号 2097-1842(2023)03-0682-19

Phase-extracting method of optical frequency scanning interference signals based on the CEEMD-HT algorithm

YANG Ke-yuan[1], DENG Zhong-wen[2*], CHEN Wen-jun[3], YAO Xin[1], SUN Hai-feng[3], SHEN Li-rong[3]

（1. *China Academy of Space Technology (Xi'an)*, *Xi'an*, 710100 *China*;
2. *Academy of Advanced Interdisciplinary Research*, *Xidian University*, *Xi'an*, 710071 *China*;
3. *School of Space Science and Technology*, *Xidian University*, *Xi'an*, 710071 *China*）

* *Corresponding author*, *E-mail*: *zwdeng@xidian.edu.cn*

Abstract: Aiming at the problem that the optical frequency scanning nonlinearity affects the phase extracting accuracy of the optical Frequency Scanning Interferometry (FSI) signal, and thus reduces the FSI ranging accuracy, a phase-extracting method based on the Complementary Ensemble Empirical Mode Decomposition and Hilbert Transform (CEEMD-HT) algorithm is proposed in this paper. Based on theoretical derivation and simulation analysis of the CEEMD-HT algorithm, the effectiveness of the algorithm in solving the phase of the non-stationary interference signal in scanning-frequency is verified by simulation. Further simulation experiments were implemented by using the real output optical frequency obtained with FSI ranging system as the simulation conditions. The simulation results showed that the CEEMD-HT algorithm significantly improved the phase extracting accuracy of the interference signal and the FSI ranging accuracy. Finally, the proposed interference signal phase-extracting method was verified via the experiment of the FSI ranging system. The results showed that the ranging repeatability of the measurement system based on the CEEMD-HT algorithm was 2.79 μm in the free space measurement range of 2 m. Compared with EMD-HT and direct measurement methods, the ranging repeatability was improved by 5.19 times and 8.28 times, respectively.

Key words: interferometry measurement; ranging measurement; frequency scanning; nonlinearity in frequency scanning; phase extracting

---

收稿日期:2022-07-27; **修订日期**:2022-09-02

基金项目:国家自然科学基金(No. 52205576);陕西省自然科学基础研究计划(No. 2021JQ-187);中央高校基本科研业务费专项资金(No. XJS212203)

Supported by National Natural Science Foundation of China (No. 52205576); Natural Science Basic Research Program of Shaanxi Province (No. 2021JQ-187); Foundamental Research Funds for the Central Universities (No. XJS212203)

基于互补集合经验模态分解结合希尔伯特变换的光频扫描干涉信号相位提取方法

杨克元[1], 邓忠文[2*], 陈文军[3], 姚　鑫[1], 孙海峰[3], 沈利荣[3]
（1. 中国空间技术研究院 西安分院, 陕西 西安 710100;
2. 西安电子科技大学 前沿交叉研究院, 陕西 西安 710071;
3. 西安电子科技大学 空间科学与技术学院, 陕西 西安 710071）

摘要: 光频扫描非线性会影响光频扫描干涉(FSI)信号的相位提取精度, 进而降低扫频干涉测距精度。针对这一问题, 本文提出了一种基于互补集合经验模态分解结合希尔伯特变换(CEEMD-HT)算法的干涉信号相位提取方法。在 CEEMD-HT 算法进行理论推导和仿真分析的基础上, 通过仿真验证了该算法对非平稳扫频干涉信号相位求解的有效性。进一步采用 FSI 实验系统中的真实输出光频率作为仿真条件进行了仿真实验, 仿真结果表明 CEEMD-HT 算法对干涉信号相位的求解精度以及 FSI 测距精度都有显著的改善。最后, 通过 FSI 测距系统的测距实验对所提出的干涉信号相位提取方法进行验证。结果表明: 在 2 m 自由空间测量范围内, 基于 CEEMD-HT 算法的重复测距精度为 2.79 μm, 相较于 EMD-HT 和直接测量法分别提高了 5.19 倍和 8.28 倍。

关　键　词: 干涉测量; 距离测量; 光频扫描; 扫频非线性; 相位提取
中图分类号: TH741.1　　**文献标志码:** A　　**doi:** 10.37188/CO.2022-0173

1　Introduction

The optical Frequency Scanning Interferometry (FSI)-based absolute ranging technology has broad application prospects in many fields, such as multi-satellite formation, large-scale equipment assembly and manufacturing, and automatic driving[1-9]. The typical light source of the FSI ranging system is an External Cavity Diode Laser (ECDL), which continuously tunes the optical frequency by changing the length of the external cavity through piezoelectric ceramics or motors. However, due to the nonlinear response of the displacement tuning element, the optical frequency change of the ECDL output is nonlinear with time under the linear drive signal input[10-12]. The nonlinearity in optical frequency scanning of ECDL leads to the frequency time-varying characteristics of the FSI interference signal, which in turn affects the phase extracting accuracy of the interference signal, and finally leads to the decrease of FSI ranging accuracy[2, 11, 13-14]. Therefore, reducing the influence of optical frequency scanning nonlinearity on interference signals is essential to improve the ranging accuracy of FSI.

The current research methods for the nonlinearity in optical frequency scanning of ECDL can be summarized into the following two categories: one type of method is to realize the early suppression of frequency scanning nonlinearity by monitoring the optical frequency change information and using the feedback loop to control the optical frequency scanning rate online. For example, in 2009, Roos P A *et al*..[15] used the double phase-locked loop method to control the optical frequency scanning rate of ECDL online, reducing the influence of scanning nonlinearity on the frequency of interference signals, and achieving a ranging accuracy of 86 nm in the range of 1.5 m. This method suppresses the scanning nonlinearity before the optical path forms interference by introducing a feedback control loop. However, the introduction of feedback control loop increases the system complexity, and the loop bandwidth also limits the increase in optical frequency scanning rate; another type is to eliminate the influence of frequency scanning nonlinearity on the

phase extracting accuracy of interference signal by sampling and post-processing the frequency time-varying interference signal. For example, in 2014, SHI G *et al*..[2] constructed an all-fiber Mach-Zehnder reference interferometer with a 30 m optical path difference, which uses the generated reference interference signal to resample the measurement interference signal at equal optical frequency intervals, thus greatly reducing the influence of scanning nonlinearity on the interference signal measurement and improving the spatial resolution of the ranging system by about 30 times. However, in such resampling methods, the reference interference signal used for resampling needs to satisfy the Nyquist sampling theorem, which leads to the limitation of the system measurement range by the optical path difference of the reference interferometer. In addition, the introduction of the reference interferometer also increases the complexity of the ranging system.

Both of the above two types of methods increase the system complexity in different extent, and limit the measurement bandwidth and measurement range of the ranging system. To this end, in 2018, DENG W *et al*..[16-18] proposed that Empirical Mode Decomposition (EMD) combined with Hilber Transform (HT) to perform phase extracting of non-stationary interference signals, which effectively reduced the influence of the optical frequency scanning nonlinearity on the phase extracting accuracy of interference signals. However, traditional EMDs have component mode aliasing when decomposing and reconstructing nonstationary signals, which limits the further improvement of phase extracting accuracy. Therefore, in this paper, the non-stationary signal mode decomposition reconstruction method based on noise-assisted data analysis method-Complementary Ensemble Empirical Mode Decomposition (CEEMD) is used to decompose and reconstruct the measurement interference signal, improve the modal aliasing caused by the traditional EMD method, and further reduce the influence of the optical frequency scanning nonlinearity.

2 Theoretical derivation

2.1 FSI ranging principle

As shown in Fig. 1, the FSI ranging system outputs a frequency scanning laser from ECDL, which is divided into two beams at the beam splitter (BS1) after being collimated: one beam enters the Fabry-Perot (F-P) Etalons, and the transmitted F-P signal is generated by photodetector (PD1); the other enters the Michelson interference light path and is divided into reference light and measurement light by the beam splitter (BS2). After being reflected by the reflecting prism RR1 and RR2, the interference signal is formed on the photodetector (PD2).

In FSI ranging system, the output optical frequency of ECDL $\upsilon(t)$ can be expressed as:

$$\upsilon(t) = \upsilon_0 + \beta \cdot t \quad , \tag{1}$$

where υ_0 is the initial optical frequency output by

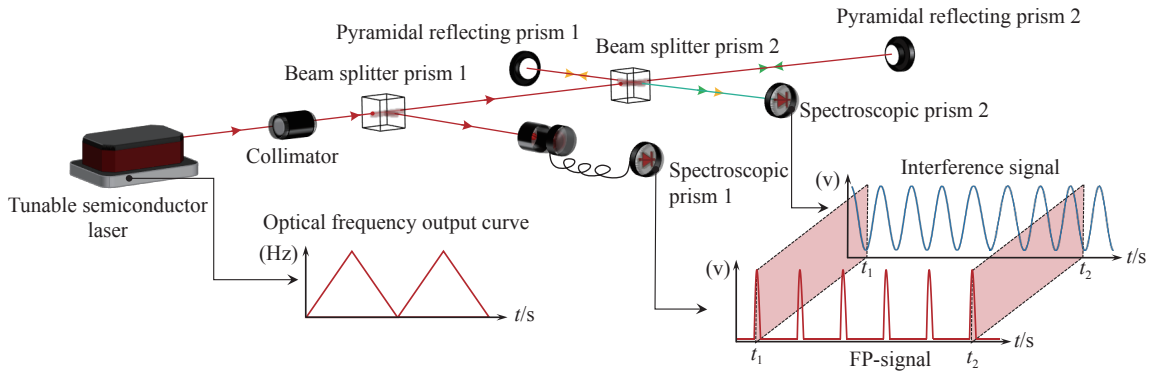

Fig. 1 Schematic of the FSI ranging system

图 1 FSI 测距系统原理示意图

the laser, and β is the optical frequency scanning rate. According to the principle of light wave interference, the interference signal can be expressed as:

$$I(t) = I_r + I_m + 2\sqrt{I_r \cdot I_m}\cos[2\pi\upsilon_0\tau + 2\pi\beta\cdot\tau\cdot t] \quad , \tag{2}$$

where I_r is the light intensity of the reference light, I_m is the light intensity of the measurement light, and τ is the delay of the measurement light relative to the reference light in the time domain. According to Eq. (2), the instantaneous phase of the interference signal φ is expressed as:

$$\varphi = 2\pi\upsilon_0\tau + 2\pi\beta\cdot\tau\cdot t \quad . \tag{3}$$

If the optical frequency variation of ECDL is $\Delta\upsilon$ within the period $\Delta t=t_2-t_1$, the corresponding phase difference $\Delta\varphi$ can be expressed as follows:

$$\Delta\varphi = \varphi(t_2) - \varphi(t_1) = 2\pi\cdot\tau\cdot\beta\cdot\Delta t \quad . \tag{4}$$

In combination with equation (1), the phase difference $\Delta\varphi$ can be further rewritten as follows:

$$\Delta\varphi = 2\pi\cdot\tau\cdot[\upsilon(t_2) - \upsilon(t_1)] = 2\pi\cdot\tau\cdot\Delta\upsilon \quad . \tag{5}$$

When the distance to be measured is L, the delay τ can be expressed as:

$$\tau = \frac{2n\cdot L}{c} \quad , \tag{6}$$

where n is the refractive index of air and c is the velocity of light. The expression of distance L to be measured can be obtained by connect equations (5) with (6):

$$L = \frac{c\cdot\tau}{2n} = \frac{c\cdot\Delta\varphi}{4\pi\cdot n\cdot\Delta\upsilon} \quad . \tag{7}$$

2.2 Nonlinearity analysis of FSI scanning frequency

It can be seen from Equation (7) that the ranging accuracy of the system depends on the extraction of the phase difference $\Delta\varphi$ of the interference signal and the calculation of the optical frequency variation range $\Delta\upsilon$. The optical frequency variation range can be obtained by counting the number of F-P signal peaks in Fig. 1, and after selecting the starting and ending F-P peaks, the relationship between the optical frequency variation range $\Delta\upsilon$ and the F-P peak number r is as follows:

$$\Delta\upsilon = (r-1)\cdot FSR \quad , \tag{8}$$

where FSR is the Free Spectrum Range (FSR) of the Fabry Perot etalon, that is, the corresponding optical frequency difference between adjacent peaks. Therefore, solving the interference signal phase difference $\Delta\varphi$ corresponding to the scanning range $\Delta\upsilon$ is the key to determine the ranging accuracy of FSI.

In fact, the interference signal intercepted by the F-P signal includes an integer period signal segment and a fractional period signal segment, and the corresponding phase difference between two adjacent peaks in the integer period signal segment is 2π, so the integer periodic phase difference can be directly solved by the number of peaks of the interference signal. As shown in Figure 2, in order to improve the solving efficiency of the interference signal phase difference, the interference signal phase difference is divided into three parts, that is, integer phase difference $\Delta\varphi_i$, starting decimal phase difference $\Delta\varphi_s$ and cutoff decimal phase difference $\Delta\varphi_e$. When the phase segment is automatically intercepted, from the moment t_s of the starting F-P peak, the segment is intercepted to the right to the moment t_{p1} of the first wave peak , which corresponds to the starting decimal phase difference interval; similarly, from the moment t_e at which the F-P peak is termin-

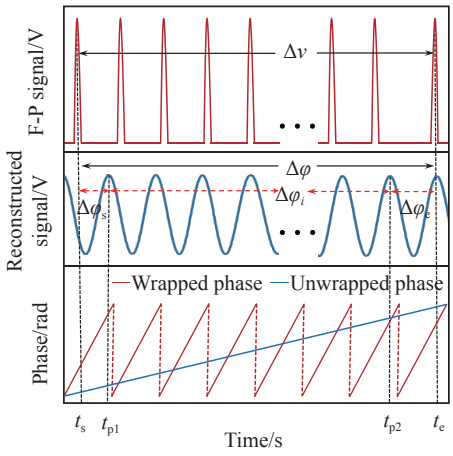

Fig. 2　Schematic diagram of the interferometric phase decomposition

图 2　干涉信号的相位分解示意图

ated, the segment is intercepted to the left to the moment t_{p2} at which the last wave peak is, which is the interval of the cut-off decimal phase. The interval from t_{p1} to t_{p2} is the integer phase interval. The integer phase difference $\Delta\varphi_i$ can be expressed as:

$$\Delta\varphi_i = (\delta - 1)\cdot 2\pi \quad . \tag{9}$$

The integer phase difference is determined by the peak number δ of the interference signal, the decimal phase difference is $\Delta\varphi_s$, and $\Delta\varphi_e$ is solved by HT:

$$\begin{cases} \Delta\varphi_s = \varphi_u(t_{p1} - t_s)/T \\ \Delta\varphi_e = \varphi_u(t_e - t_{p2})/T \end{cases} , \tag{10}$$

where φ_u is the phase unwrapping function after HT, and T is the period of the interference signal. Thus, the phase of the interference signal can be expressed as:

$$\Delta\varphi = \Delta\varphi_i + \Delta\varphi_s + \Delta\varphi_e \quad . \tag{11}$$

At this time, the scanning frequency range $\Delta\upsilon$ and the phase difference $\Delta\varphi$ of its corresponding interference signal can be substituted into Eq. (7) to get the distance L.

However, the displacement tuning element PZT of ECDL has hysteresis and creep characteristics, resulting in a nonlinear relationship between the optical frequency change output by the ECDL and the time under the linear driving signal input. The optical frequency scanning rate β is no longer a fixed value, and the interference signal period T becomes a time variable, and an error will occur when calculating the decimal phase using HT. Therefore, this paper proposes to use the CEEMD-HT algorithm to calculate the decimal phase value point-by-point in the intercepted interference signal segment, and then calculate the phase change of the intercepted interference signal, so as to avoid the impact of scanning nonlinearity on its phase calculation.

2.3 Phase extracting principle based on CEEMD-HT

Firstly, the phase solving method of HT in FSI interference signal is derived, and for any signal $x(t)$, its HT can be expressed as:

$$H[x(t)] = \mathcal{F}^{-}[\mathcal{F}(x(t))\delta(\omega)] \quad , \tag{12}$$

where $\mathcal{F}[\cdot]$ and $\mathcal{F}^{-}[\cdot]$ are the Fourier transform and the inverse Fourier transform, and $\delta[\omega]$ is the window function of HT, which can be expressed as:

$$\delta(\omega) = -j\,\mathrm{sgn}(\omega) = \begin{cases} -j\ (\omega > 0) \\ 0\ (\omega = 0) \\ j\ (\omega < 0) \end{cases} . \tag{13}$$

According to Eq. (2), the $I(t)$ expression of FSI interference signal can be simplified as follows:

$$I(t) = a(t) + b(t)\cos\varphi(t) \quad , \tag{14}$$

where $a(t)$ is the DC component of the interference signal, $b(t)$ is the amplitude modulation of the interference signal, and the phase information of the interference signal is hidden in $b(t)\cos\varphi(t)$. Use a suitable high pass filter to filter out the low-frequency DC term $a(t)$, and get the term $b(t)\cos\varphi(t)$ containing the phase information of the interference signal. The interference signal can be expressed as follows:

$$I_p(t) = \mathcal{F}^{-}[\mathcal{F}[I(t)]\cdot W(\omega)] = b(t)\cos\varphi(t) \quad , \tag{15}$$

where $W(\omega)$ is the window function of the high pass filter. In addition, BEDROSIAN E[17] *et al*.. have made a detailed discussion on the HT in the form of product, and obtained an important conclusion: the HT of the product of low-pass signal and high-pass signal is equivalent to the product of the HT of low-pass signal and high-pass signal. Based on this conclusion, the HT of the interference signal after high-pass filtering can be expressed as:

$$H[I_p(t)] = b(t)H[\cos\varphi(t)] = b(t)\sin\varphi(t) \quad . \tag{16}$$

Based on the above analysis, the HT is used to construct the analytic function $\hat{I}(t)$ of the interference signal:

$$\hat{I}(t) = I_p(t) + iH[I_p(t)] \quad . \tag{17}$$

Combining equations (15) and (16), we can get:

$$\hat{I}(t) = b(t)\cos\varphi(t) + ib(t)\sin\varphi(t) \quad . \tag{18}$$

The phase function $\varphi(t)$ of the interference signal can be expressed as:

$$\varphi(t)=\arctan\left[\frac{\mathrm{Im}(\hat{I}(t))}{\mathrm{Re}(\hat{I}(t))}\right]=\arctan\left[\frac{b(t)\sin\varphi(t)}{b(t)\cos\varphi(t)}\right] \quad . \tag{19}$$

According to Eq. (19), the phase change of interference signal $I(t)$ from time t_1 to t_2 can be expressed as:

$$\Delta\varphi=\varphi_{\mathrm{u}}(t_2)-\varphi_{\mathrm{u}}(t_1) \quad . \tag{20}$$

It should be noted that the Signal-to-Noise Ratio (SNR) of the interference signal is a key factor affecting the accuracy of HT phase solution[16]. The interference signal is affected by the measurement environment perturbation, photodetector noise and other factors, especially under long-distance measurement conditions, and its SNR is often low, so here the EMD is used to perform adaptive decomposition of the interference signal and reconstruct a high-quality interference signal to improve the interference signal phase extracting accuracy. In the signal decomposition, EMD does not depend on the basis function, and the adaptive decomposition is performed completely according to the extreme point distribution of the signal itself, which decomposes the complex signal containing multiple frequency components into the sum of multiple single frequency components step by step. For the analysis and processing of complex signals with non-stable characteristics, the specific process of EMD decomposition is described as follows:

(1) Firstly extract the upper and lower extreme points of the original signal $s(t)$, and fit the upper and lower extreme points with triple spline fitting to obtain the upper envelope signal $e_{\mathrm{u}}(t)$ and the lower envelope signal $e_{\mathrm{d}}(t)$.

(2) Find the mean envelope signal $m(t)$ of the upper and lower envelopes, remove $m(t)$ from the initial signal $s(t)$, we obtain the signal $c(t)$.

(3) Treat $c(t)$ as a new $s(t)$ signal and repeat steps (1)-(2) until the latest decomposed $c(t)$ satisfies the decomposition termination condition[17], at which point $c(t)$ is considered a first-order component IMF_1.

(4) Remove IMF_1 from $s(t)$, record the remaining signal as $r(t)$, treat $r(t)$ as a new $s(t)$ signal, repeat steps (1)-(3), and obtain the components IMF_i of each order in turn.

The decomposition of nonstationary signal $s(t)$ can be expressed as:

$$s(t)=\sum_{i=1}^{n}IMF_i+r_n(t) \quad , \tag{21}$$

where IMF_1, $IMF_2,\cdots$, IMF_n are the components of each order obtained by EMD, also known as the Intrinsic Modal Function (IMF), and Fig. 3 shows a schematic diagram of the decomposition reconstruction of the measured nonstationary interference signal by EMD.

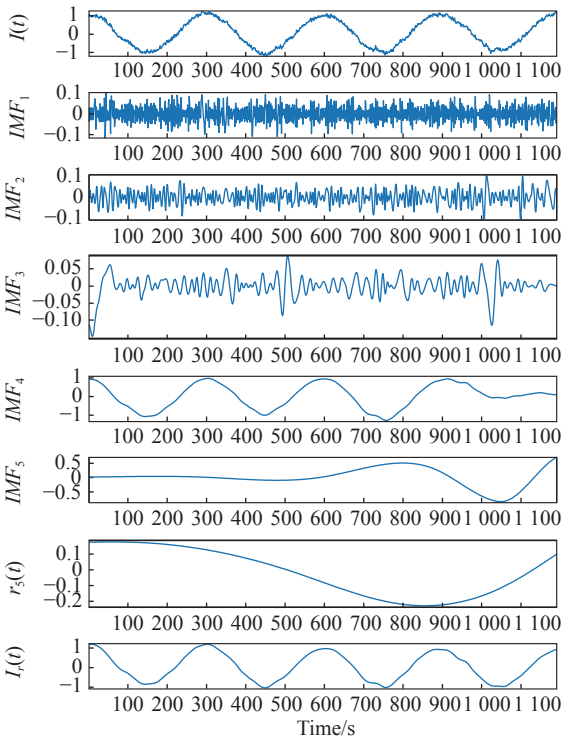

Fig. 3　Schematic diagram of the EMD decomposition and reconstruction of the non-stationary interference signal

图 3　EMD 对非稳干涉信号的分解重构示意图

Ideally, each IMF contains only one characteristic frequency. However, in the process of signal decomposition, different characteristic frequencies are mixed in the same IMF component, or the same characteristic frequency exists in different IMF components. Wu and Huang *et al.*.[19] define this

phenomenon as modal aliasing. Due to the existence of modal aliasing, the two adjacent IMF components obtained by EMD will interfere with each other, and the characteristic frequency mixing cannot be distinguished. Therefore, in the process of decomposition and reconstruction of non-stationary signals, it is inevitable to eliminate the true component of the signal itself or introduce the false component into the reconstructed signal, which seriously affects the quality of signal reconstruction. As IMF_4 shown in Figure 3, we generally regard this component as the most important component reflecting the characteristics of the interference signal. Obviously, due to the influence of modal aliasing, other frequency components are mixed into the component IMF_4, which leads to certain fluctuations in the time domain. Therefore, it directly affects the quality of the reconstructed interference signal $I_r(t)$, and then affects the phase extracting accuracy of the interference signal.

In order to overcome the modal aliasing problem, YEH J R *et al*..[20] proposed the CEEMD algorithm based on EMD. The CEEMD algorithm successively adds pairs (one positive and one negative) of white noise to the original signal, and then performs EMD separately. The algorithm flow is shown in Figure 4. The CEEMD algorithm uses the characteristics of uniform distribution of white noise in the time-frequency space, and the component signal IMF_i of different time-frequency scales is automatically mapped to the appropriate time-frequency scale related to it through the white noise background, to ensure the continuity of each component in the time domain and reduce modal aliasing. In addition, using the time-domain zero mean characteristic of white noise, the CEEMD algorithm eliminates the influence of the added white noise on the original signal by adding white noise pairs multiple times and averaging multiple groups of IMF components of the same order.

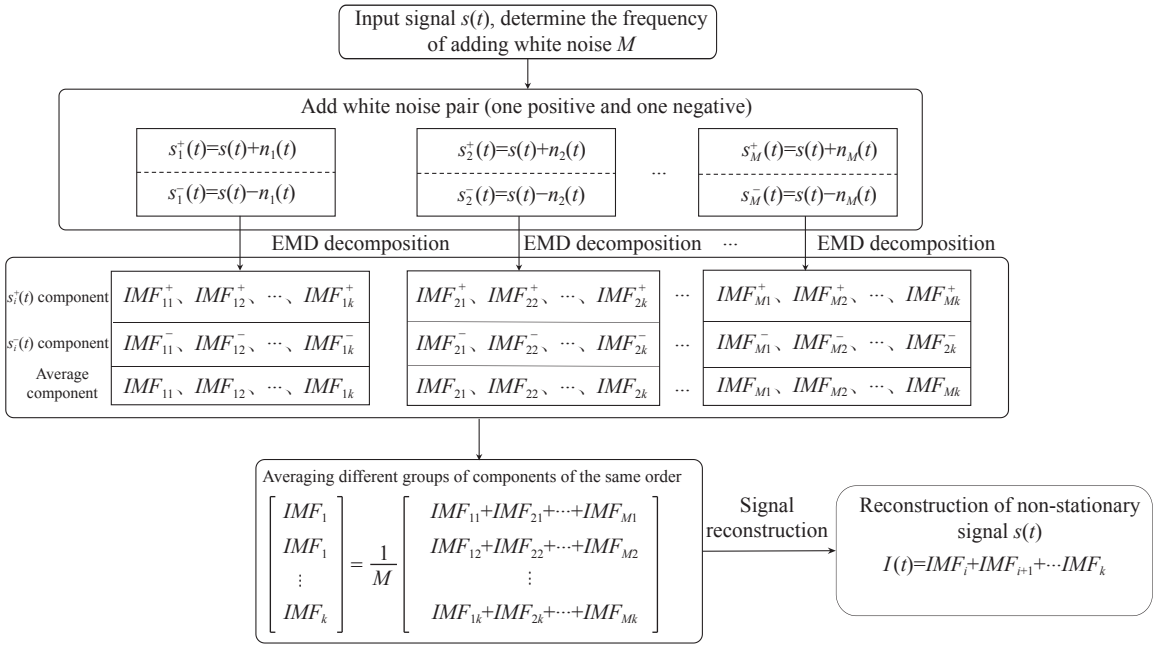

Fig. 4 Schematic diagram of CEEMD algorithm flow

图 4 CEEMD 算法流程示意图

The following is the detailed process of CEEMD algorithm decomposition and reconstruction. First, add white noise signal $n(t)$ in pairs to the original signal $s(t)$, that is:

$$\begin{bmatrix} s_{j1}(t) \\ s_{j2}(t) \end{bmatrix} = \begin{bmatrix} 1 & 1 \\ 1 & -1 \end{bmatrix} \begin{bmatrix} s(t) \\ n_j(t) \end{bmatrix} . \tag{22}$$

The synthesized signals of the original signal $s(t)$ after the jth addition of white noise pairs are

$s_{j1}(t)$ and $s_{j2}(t)$, respectively, and EMD of $s_{j1}(t)$ and $s_{j2}(t)$ will respectively obtain two sets of n-layer IMF components, namely:

$$\begin{bmatrix} s_{j1}(t) \\ s_{j2}(t) \end{bmatrix} = \begin{bmatrix} IMF_{j1,1} & IMF_{j2,1} \\ IMF_{j1,2} & IMF_{j2,2} \\ \vdots & \vdots \\ IMF_{j1,n} & IMF_{j2,n} \\ r_{j1,n}(t) & r_{j2,n}(t) \end{bmatrix}^{\mathrm{T}} . \tag{23}$$

Averaging components of the same order of each layer, we can get:

$$s_j(t) = \begin{bmatrix} \dfrac{IMF_{j1,1} + IMF_{j2,1}}{2} \\ \dfrac{IMF_{j1,2} + IMF_{j2,2}}{2} \\ \vdots \\ \dfrac{IMF_{j1,n} + IMF_{j2,n}}{2} \end{bmatrix} . \tag{24}$$

When, in Eqs. (22), (23) and (24), $j = 1, 2, \cdots, m$, the component matrix of row n and column m can be obtained, that is:

$$\begin{bmatrix} s_1 \\ s_2 \\ \vdots \\ s_j \end{bmatrix} = \begin{bmatrix} IMF_{1,1} & IMF_{2,1} & \cdots & IMF_{m,1} \\ IMF_{1,2} & IMF_{2,2} & \cdots & IMF_{m,2} \\ \vdots & \vdots & \ddots & \vdots \\ IMF_{1,n} & IMF_{2,n} & \cdots & IMF_{m,n} \end{bmatrix}^{\mathrm{T}} . \tag{25}$$

The component matrix of the CEEMD decomposition signal can be obtained by averaging components of the same order of each layer in the component matrix, namely:

$$s(t) = \begin{bmatrix} \dfrac{1}{m} \cdot \sum_{j=1}^{m} IMF_{j,1} \\ \dfrac{1}{m} \cdot \sum_{j=1}^{m} IMF_{j,2} \\ \vdots \\ \dfrac{1}{m} \cdot \sum_{j=1}^{m} IMF_{j,n} \end{bmatrix} = \begin{bmatrix} IMF_1 \\ IMF_2 \\ \vdots \\ IMF_n \end{bmatrix} . \tag{26}$$

Fig. 5 shows the decomposition and reconstruction results of the measured interference signal by CEEMD algorithm. The components of each order are arranged in order from high frequency to low frequency. By removing the high frequency false components and residual components, the remaining real components are reconstructed to obtain the reconstructed interference signal $I_r(t)$ with high SNR.

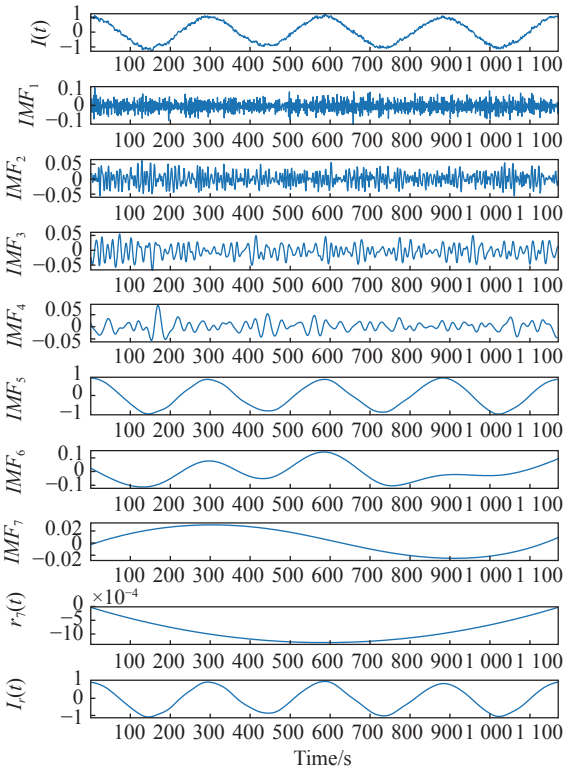

Fig. 5　Schematic diagram of the decomposition and reconstruction of the interference signal via CEEMD

图 5　CEEMD 对干涉信号的分解重构示意图

Compared with the EMD algorithm, CEEMD algorithm decomposes more components and distinguishes the characteristics between components more clearly, which indicates that CEEMD algorithm can reduce the mutual interference between adjacent IMFs to a certain extent. Comparing the quality of the reconstructed interference signal $I_r(t)$ in Fig. 3 and Fig. 5, the reconstruction quality of the interference signal by the CEEMD algorithm is better than that by the EMD algorithm. Obviously, CEEMD algorithm will help improve the phase solving accuracy of the interference signal. Next, we will verify the effectiveness of the CEEMD algorithm through simulation and experiments.

3　Experimental results

3.1　Setting of FSI system experiment platform

The FSI ranging platform and experimental re-

lated equipment constructed in this experiment are shown in Fig. 6. ECDL (TLB-6712, Newport) and data acquisition card (PXIe-5105, National Instruments) are controlled by the host computer, the frequency modulation range of ECDL is set to 765−775 nm, and the frequency modulation speed is set to 2 nm/s. The optical fiber splitter (TN785R3A1, Thorlabs) divides the light source into two channels, which are coupled to the free space through the collimator (F230APC-780, Thorlabs), and 25% of the light enters the FP etalon (SA200-5B, Thorlabs). The FP signal is detected by the built-in photodetector of the FP etalon, and filtered and amplified by the FP controller; 75% of the light enters the measuring optical path. After passing through the Michelson interference optical path, interference is formed at PD (Model 1801, Newport), and the PD converts the optical interference signal into a voltage signal. DAQ collects FP signal and interference signal synchronously, and the acquired signal will be processed by PC to complete ranging.

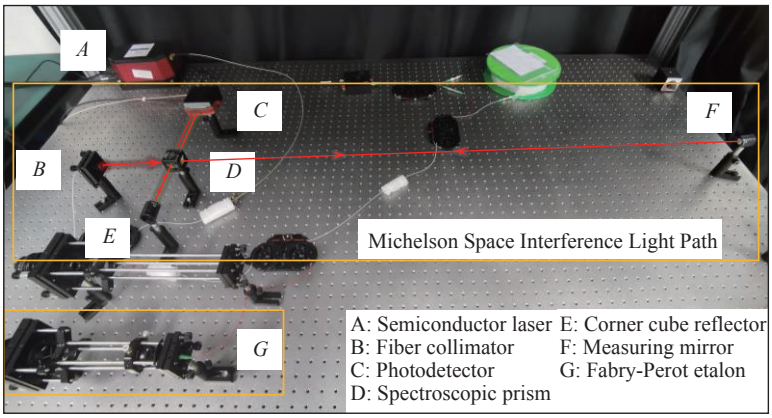

Fig. 6 Schematic diagram of the FSI experimental system

图 6 FSI 实验系统示意图

3.2 FSI simulation parameter setting

To verify the effectiveness of the algorithm, in this paper, the peak point of the transmission signal obtained from the F-P etalon is fitted to obtain the actual optical frequency change curve $\upsilon(t)$ of ECDL output. The optical frequency change rate β of ECDL output can be expressed as:

$$\beta(t)=\frac{\mathrm{d}\upsilon(t)}{\mathrm{d}t} \quad . \tag{27}$$

Substituting equation (27) into Eq. (2), and adding noise $n_p(t)$ to the simulated interference signal, the final form of the simulated interference signal is obtained as:

$$I'(t)=a\cdot\cos\left[2\pi(\upsilon_0+\beta(t)\cdot t)\cdot\frac{2n\cdot L}{c}\right]+b\cdot n_p(t) \quad , \tag{28}$$

where a and b are amplitudes of the simulated interference signal and noise respectively.

The simulation parameter settings are shown in Table 1.

Tab. 1 Simulation parameters of the scanning nonlinearity

表 1 扫频非线性仿真参数

Parameters	Parameter name	Value/unit
a	Interference signal amplitude	1 V
υ_0	ECDL initial optical frequency	0 Hz
$\Delta\upsilon$	Optical frequency scanning range	2 THz
L	Measured distance	10 m
n	Air refractive index	1
c	Velocity of light	3×10^8 m/s
t	Scan cycle	5 s
SNR	Signal to noise ratio of interference signal	25, 20, 15, 10 dB
S	Interference signal sampling frequency	10 MHz

3.3　FSI simulation experiment results

In this section, we will compare and verify the ranging performance of CEEMD-HT algorithm and EMD-HT algorithm based on the analysis in Chapter 2 as the theoretical basis. First, we extracted the single cycle phase difference of the interference signal under different signal-to-noise conditions for 20 times and compared the extracted results with the standard single cycle phase difference to reflect the extraction capability of the above two algorithms for decimal cycle phase. As shown in Fig. 7 (color online), both algorithms can reduce the extraction error and standard deviation of the single cycle phase difference compared with the direct extraction of the single cycle phase difference, and under different signal-to-noise conditions, the extract effect of the single cycle phase difference by the CEEMD-HT algorithm is better than that by the EMD-HT algorithm.

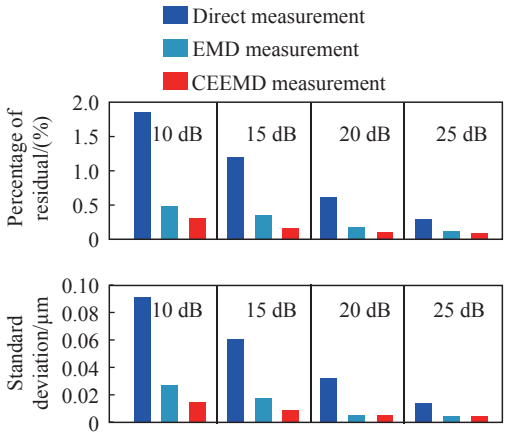

Fig. 7　Comparison of simulation results of single cycle phase difference extraction

图 7　单周期相位差提取仿真结果对比图

Next, to verify the overall measurement performance of the CEEMD-HT algorithm, we have applied the CEEMD-HT algorithm and the EMD-HT algorithm to perform 500 repeated rangings under different SNR conditions and compared them with the standard distance of 10 m set by simulation. The histograms of the measurement residuals and the measurement standard deviation obtained under different SNR conditions are shown in Fig. 8 (color online). The results show that both the CEEMD-HT algorithm and the EMD-HT algorithm can improve the ranging performance of the FSI to some extent compared with the direct measurement.

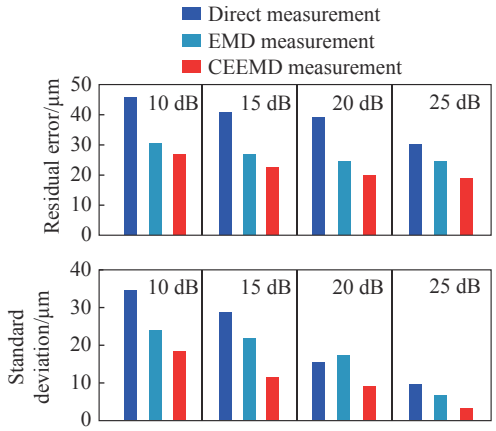

Fig. 8　Comparison of the ranging simulation results of different phase extracting methods

图 8　测距仿真结果对比图

It is worth noting that when the SNR of the simulated interference signal is 20 dB, the EMD-HT algorithm does not show significant measurement advantages compared with direct measurement. Combined with Fig. 3 and the principle of EMD decomposition reconstruction, it can be seen that EMD depends on the extreme point distribution of the interference signal when decomposing the interference signal, and when the SNR of the simulated interference signal is relatively increased, the volatility of the extreme point distribution decreases, which will aggravate the modal aliasing and have a certain impact on the decomposition performance of the EMD algorithm. Therefore, when the interference signal is reconstructed, some high-frequency noise components will be mixed into the reconstruction signal, and some of the real components of the interference signal will be lost, which will then have a certain impact on the extraction of the phase difference. In addition, combined with the analysis in Chapter 2, when dividing the phase segment, it also depends on the extreme point distribution of the interference signal, so the smoothness of the reconstruction interference signal in the time domain will have a corresponding impact on the interception of the signal seg-

ment, which in turn affects the stability of the extraction of the phase difference, resulting in the relative decrease of the measurement stability of the EMD algorithm under this the 20 dB SNR.

Compared with the EMD algorithm, during the decomposition of the interference signal, CEEMD adds white noise pairs to the interference signal to be decomposed, which makes the fluctuation degree of the interference signal with different SNRs in the time domain tend to be consistent. Therefore, the decomposition and reconstruction performance of the CEEMD algorithm is relatively less affected by the SNR. From the simulated ranging results shown in Fig. 8, it can be seen that the measurement residuals and standard deviations of the CEEMD-HT algorithm are lower than those of the EMD-HT algorithm and direct measurements under a certain interference signal SNR. It is worth noting that the CEEMD-HT algorithm can improve the repeatability of the system measurement more effectively than to improve the accuracy of the system measurement. The standard deviation of the CEEMD-HT measurement is 3.14 μm at a SNR of 25 dB for the interference signal and a range of 10 m.

In addition, CEEMD needs to add noise and perform EMD for many times when processing interference signals, which increases the complexity of the algorithm and reduces the efficiency of signal processing to a certain extent. In view of this, the measurement time and efficiency of the CEEMD-HT algorithm are evaluated and analyzed. As shown in Fig. 9 (color online), the measurement

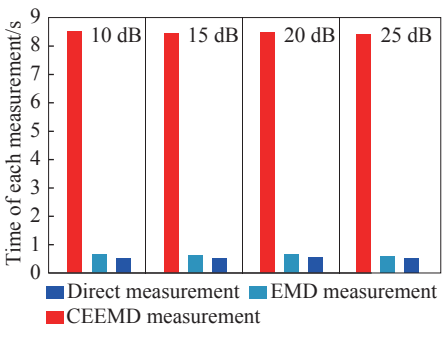

Fig. 9 Comparison of single measurement time

图 9 单次测量用时对比图

efficiency of the CEEMD-HT algorithm is lower than that of the EMD-HT algorithm and direct measurement under the same measurement conditions.

In summary, the CEEMD-HT algorithm can improve the signal processing performance while its simplicity and processing efficiency are also affected accordingly, and it cannot simultaneously take into account the stability and rapidity of the system measurement. However, as an adaptive signal processing means, it can still improve the stability and anti-interference capability of the FSI system without increasing the complexity and cost of the system, which has certain positive significance to improve the performance of the FSI system.

3.4 Experiments and results

The FSI ranging experimental system is shown in Fig. 6. The sampling rate of the data acquisition device is set to 10 MS/s, and the single sampling time is 5 s, and the FP signal and the interference signal are acquired simultaneously. After the phase segment of the interference signal is divided, the CEEMD-HT algorithm and EMD-HT algorithm are applied to decompose and reconstruct the interference signal of the decimal phase segment respectively, the phase difference of the reconstructed signal is solved, and finally the optical frequency variation range $\Delta\upsilon$ and the phase difference of the intercepted interference signal $\Delta\varphi$ are substituted into the ranging Eq. (7) for ranging.

Before the ranging, we analyzed and compared the performance of CEEMD-HT algorithm and EMD-HT algorithm to process the measured interference signal, and the results are shown in Fig. 10. The measured interference signal disturbed by noise is shown in Fig. 10 (a), and the reconstructed interference signals shown in Fig. 10 (b) and Fig. 10 (c) are obtained after processing by CEEMD algorithm and EMD algorithm. Comparing the locally amplified signals, both the CEEMD algorithm and the EMD algorithm can effectively reduce the interference of noise on the interference signal. However,

the interference signal after EMD processing still has fluctuations in the time domain, and such fluctuations will have certain effects on both of performing phase segment division and using HT for phase solution. It can be seen that the CEEMD algorithm is more effective in processing the interference signal under the same conditions.

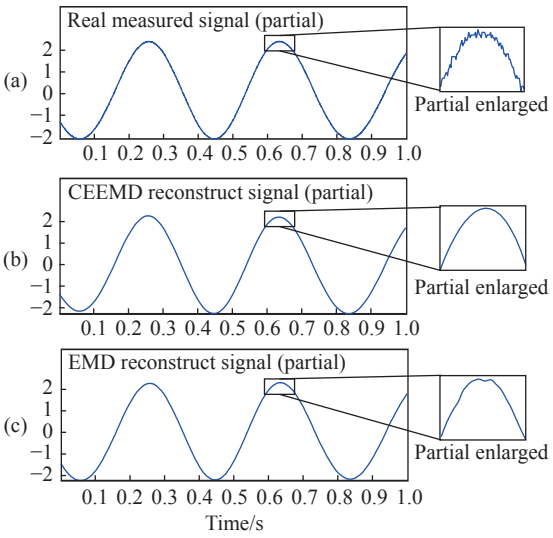

Fig. 10　Comparison of measured interference signal processing results

图 10　实测干涉信号处理对比图

Based on the above analysis, the actual measurement performance of the CEEMD-HT algorithm is experimentally verified in this section. 50 repetitive measurements are performed on the same target in the 2 m free-space range, and the ranging results are shown in Figure 11. The experimental results show that, in the measurement range of 2 m free space, the repetitive measurement standard deviation based on the CEEMD-HT algorithm is 2.79 μm, which is 5.19 times lower than the repetitive measurement standard deviation of 14.48 μm based on the EMD-HT algorithm, and is 8.28 times lower than the repetitive measurement standard deviation of 23.09 μm by the direct measurement. This shows that the CEEMD-HT algorithm can effectively improve the stability of the FSI system ranging and the anti-interference capability of the system.

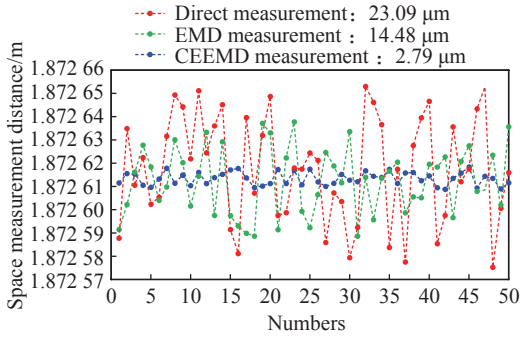

Fig. 11　Experiment results of the FSI ranging measurement

图 11　FSI 实验测距结果

4　Conclusion

Based on the analysis of the effect of optical frequency scanning nonlinearity on the ranging accuracy of the FSI system, we propose a CEEMD-HT-based interference signal phase solving method, and conducts theoretical derivation and simulation analysis on the application feasibility of the CEEMD-HT algorithm in interference signal phase solving. To verify the effectiveness of the CEEMD-HT algorithm for phase solution of non-stationary interference signals, simulation experiments are conducted using the real output optical frequency in the FSI experimental system as the simulation conditions. The simulation results show that the performance of the CEEMD-HT algorithm outperforms that of the direct measurement and EMD-HT algorithm for both single-cycle phase extracting and overall measurement. The standard deviation of the CEEMD-HT algorithm is 3.14 μm in the 10 m range. The measurement efficiency of the algorithms is compared, and the results show that the CEEMD-HT algorithm is inferior to the direct measurement and EMD-HT algorithms in terms of measurement efficiency, and it cannot take into account both the measurement stability and measurement efficiency of the system. In addition, the FSI ranging system was used to verify the measurement results, which showed that, in the measurement range of 2 m free space, the 2.79 μm standard deviation obtained by the CEEMD-HT algorithm is 5.19

times and 8.28 times lower than that of the EMD-HT algorithm and the direct measurement method, respectively. Therefore, the CEEMD-HT algorithm can effectively reduce the effects of optical frequency scanning nonlinearity and noise on the phase extracting and ranging stability of the interference signal, and improve the anti-interference and robustness of the FSI ranging system.

——中文对照版——

1 引 言

光频扫描干涉（Frequency Scanning Interferometry, FSI）绝对测距技术在多卫星编队、大型装备装配制造、自动驾驶等领域有着广泛的应用前景[1-9]。FSI 测距系统的典型光源为窄线宽可调谐外腔半导体激光器 (External Cavity Diode Laser, ECDL), 其通过压电陶瓷或电机改变外腔长度实现对光频率的连续调谐。然而, 受到位移调谐元件非线性响应的影响, 在线性驱动信号输入下, ECDL 输出的光频率变化与时间呈非线性关系[10-12]。ECDL 的光频扫描非线性导致 FSI 干涉信号的频率时变特性, 进而影响了干涉信号相位的提取精度, 最终导致了 FSI 测距精度下降[2, 11, 13-14]。因此, 降低光频扫描非线性对干涉信号的影响对于提高 FSI 测距精度至关重要。

当前针对 ECDL 的光频扫描非线性问题的研究方法可归纳为以下两类: 第一类方法是通过监测光频变化信息, 并利用反馈环路对光频扫描速率进行在线控制, 实现扫频非线性的前期抑制, 如 2009 年, Roos P A 等人[15] 利用双锁相环法, 对 ECDL 的光频描速率进行在线控制, 降低了扫频非线性对干涉信号频率的影响, 在 1.5 m 范围内实现了 86 nm 的测距精度。这类方法通过引入反馈控制环路, 在光路形成干涉前对扫频非线性进行抑制, 然而引入的反馈控制环路增加了系统复杂度, 环路带宽同时也限制了光频扫描速率的提高; 另一类方法则通过对频率时变的干涉信号采样后进行后处理, 消除扫频非线性对干涉信号相位提取精度的影响, 如 2014 年, 时光等人[2] 构造了 30 m 光程差的全光纤马赫-曾德参考干涉仪, 利用生成的参考干涉信号对测量干涉信号进行等光频间隔重采样, 大幅降低了扫频非线性对测量干涉信号的影响, 将测距系统空间分辨率提高了约 30 倍。然而在此类重采样方法中, 用于重采样的参考干涉信号需要满足奈奎斯特采样定理, 导致系统测距范围受到参考干涉仪光程差的限制, 此外参考干涉仪的引入同样增加了测距系统的复杂度。

以上两类方法都不同程度地增加了系统复杂度, 并且限制了测距系统的测量带宽和测量范围等性能。直到 2018 年, 邓文等人[16-18] 提出, 使用经验模式分解 (Empirical Mode Decomposition, EMD) 结合希尔伯特变换（Hilber Transform, HT）对非平稳干涉信号进行相位提取, 该方法有效地降低了光频扫描非线性对干涉信号相位提取精度的影响。然而, 传统 EMD 在对非平稳信号进行分解重构时存在分量模态混叠现象, 限制了相位提取精度的进一步提高。为此, 本文利用基于噪声辅助分析的非平稳信号模式分解重构方法—互补集合经验模态分解 (Complementary Ensemble Empirical Mode Decomposition, CEEMD) 对测量干涉信号进行分解重构, 改善传统 EMD 方法造成的模态混叠现象, 进一步降低光频扫描非线性的影响。

2 理论推导

2.1 FSI 测距原理

如图 1 所示, FSI 测距系统由 ECDL 输出扫频激光, 经准直后在分光镜 (BS1) 处被分成两束: 一束进入法布里-珀罗（Fabry-Perot, F-P）标准具, 经光电探测器 PD1 探测产生透射 F-P 信号; 另一束进入迈克尔逊干涉光路, 并由分光镜 (BS2) 分为参考光和测量光, 分别经反射棱镜 RR1 和 RR2 反射后在光电探测器 PD2 上形成干涉信号。

在 FSI 测距系统中, ECDL 的输出光频率 $\upsilon(t)$可表示为:

$$\upsilon(t) = \upsilon_0 + \beta \cdot t \quad , \tag{1}$$

式中: υ_0为激光器输出的初始光频率, β为光频扫

描速率。根据光波干涉原理, 干涉信号可表示为:

$$I(t) = I_r + I_m + 2\sqrt{I_r \cdot I_m}\cos[2\pi\upsilon_0\tau + 2\pi\beta\cdot\tau\cdot t] \quad , \tag{2}$$

式中, I_r为参考光光强, I_m为测量光光强, τ为测量光相对于参考光在时域上的延迟。由式 (2) 可得, 干涉信号的瞬时相位φ表示为:

$$\varphi = 2\pi\upsilon_0\tau + 2\pi\beta\cdot\tau\cdot t \quad . \tag{3}$$

若在$\Delta t=t_2-t_1$ 时间内, ECDL 的光频变化量为$\Delta\upsilon$, 则对应的相位差$\Delta\varphi$可表示为:

$$\Delta\varphi = \varphi(t_2) - \varphi(t_1) = 2\pi\cdot\tau\cdot\beta\cdot\Delta t \quad , \tag{4}$$

结合式 (1), 相位差$\Delta\varphi$可进一步改写为:

$$\Delta\varphi = 2\pi\cdot\tau\cdot[\upsilon(t_2) - \upsilon(t_1)] = 2\pi\cdot\tau\cdot\Delta\upsilon \quad . \tag{5}$$

当待测距离为L时, 延时τ可表示为:

$$\tau = \frac{2n\cdot L}{c} \quad , \tag{6}$$

式中, n为空气折射率, c为光速。联立式 (5)、(6) 可得待测距离 L 的表达式:

$$L = \frac{c\cdot\tau}{2n} = \frac{c\cdot\Delta\varphi}{4\pi\cdot n\cdot\Delta\upsilon} \quad . \tag{7}$$

2.2　FSI 扫频非线性分析

由式 (7) 可知, 系统的测距精度取决于干涉信号相位差$\Delta\varphi$的提取和光频变化范围$\Delta\upsilon$的计算。光频变化范围可通过对图 1 中的 F-P 信号波峰数量计数获得, 选定起始、终止 F-P 波峰后, 光频变化范围$\Delta\upsilon$与 F-P 波峰数r间存在如下关系:

$$\Delta\upsilon = (r-1)\cdot FSR \quad , \tag{8}$$

式中, FSR为 F-P 标准具的自由光谱范围(Free Spectrum Range, FSR), 即相邻峰之间对应的光频差。因此, 求解扫频范围$\Delta\upsilon$对应的干涉信号相位差$\Delta\varphi$是决定 FSI 测距精度的关键。

事实上, 经 FP 信号截取后的干涉信号包含了整数周期信号段和小数周期信号段, 整数周期信号段内相邻两个波峰间对应的相位差为2π, 因此整数周期相位差可直接通过干涉信号的波峰数求解。如图 2 所示, 为提高干涉信号相位差的求解效率, 将干涉信号的相位差分为三部分求解, 整数相位差$\Delta\varphi_i$、起始小数相位差$\Delta\varphi_s$和截止小数相位差$\Delta\varphi_e$。在进行相位段自动截取时, 以起始 F-P 波峰所在时刻t_s为基准向右索引干涉的第一个波峰所在时刻t_{p1}, 该区间对应为起始小数相位差区间; 同理, 以终止 F-P 波峰所在时刻t_e为基准向左索引干涉的最后一个波峰所在时刻t_{p2}, 该区间则为截止小数相位区间; 而t_{p1}到t_{p2}所对应的区间即为整数相位区间。整数相位差$\Delta\varphi_i$可表示为:

$$\Delta\varphi_i = (\delta-1)\cdot 2\pi \quad . \tag{9}$$

整数相位差由干涉信号的峰值数δ决定, 小数相位差$\Delta\varphi_s$, $\Delta\varphi_e$则利用 HT 进行求解:

$$\begin{cases} \Delta\varphi_s = \varphi_u(t_{p1} - t_s)/T \\ \Delta\varphi_e = \varphi_u(t_e - t_{p2})/T \end{cases} \quad , \tag{10}$$

上式中, φ_u为经 HT 后的相位解包裹函数, T为干涉信号的周期。因此, 干涉信号的相位可表示为:

$$\Delta\varphi = \Delta\varphi_i + \Delta\varphi_s + \Delta\varphi_e \quad . \tag{11}$$

此时, 将扫频范围$\Delta\upsilon$和对应的干涉信号相位差$\Delta\varphi$代入式 (7) 即可解算得到被测距离L。

然而, ECDL 的位移调谐元件 PZT 存在迟滞和蠕变特性, 导致在线性驱动信号输入下, ECDL 输出的光频率变化与时间呈非线性关系, 光频扫描速率β不再为定值, 干涉信号周期 T 成为时变量, 利用 HT 计算小数相位时将会产生误差。因此, 本文提出利用 CEEMD-HT 算法计算所截干涉信号段内的逐点小数相位值, 进而实现所截干涉信号相位变化量的计算, 以避免扫频非线性对其相位计算的影响。

2.3　基于 CEEMD-HT 的相位提取原理

首先对 HT 在光频扫描干涉信号相位求解方法进行推导, 对于任意信号$x(t)$, 其希尔伯特变换可表示为:

$$H[x(t)] = \mathcal{F}^{-}[\mathcal{F}[x(t)]\delta(\omega)] \quad , \tag{12}$$

式 (12) 中$\mathcal{F}[\cdot]$和$\mathcal{F}^{-}[\cdot]$为傅立叶变换和傅立叶逆变换, $\delta(\omega)$为 HT 的窗函数, 其可表示为:

$$\delta(\omega) = -j\,\mathrm{sgn}(\omega) = \begin{cases} -j & (w>0) \\ 0 & (w=0) \\ j & (w<0) \end{cases} \quad . \tag{13}$$

由式 (2) 可知, FSI 干涉信号$I(t)$表达式可简化为下式:

$$I(t) = a(t) + b(t)\cos\varphi(t) \quad , \tag{14}$$

式中, $a(t)$为干涉信号的直流分量, $b(t)$为干涉信号的幅度调制, 干涉信号的相位信息隐含于$b(t)\cos\varphi(t)$

中。利用合适的高通器滤波掉低频直流项$a(t)$，得到包含干涉信号相位信息的$b(t)\cos\varphi(t)$项，此时干涉信号可表示为下式：

$$I_p(t)=\mathcal{F}^{-}[\mathcal{F}[I(t)]\cdot W(\omega)]=b(t)\cos\varphi(t) \quad , \tag{15}$$

式 (15) 中，$W(\omega)$为高通滤波器的窗函数。此外，Bedrosian E[17] 等人对乘积形式的希尔伯特变换做了详细的论述，并得到了重要结论：低通信号与高通信号乘积的希尔伯特变换等价于低通信号与高通信号希尔伯特变换的乘积。基于此结论，高通滤波后的干涉信号的希尔伯特变换可表示为：

$$H[I_p(t)]=b(t)H[\cos\varphi(t)]=b(t)\sin\varphi(t) \quad . \tag{16}$$

在上述分析的基础上，利用希尔伯特变换构造干涉信号的解析函数$\hat{I}(t)$：

$$\hat{I}(t)=I_p(t)+iH[I_p(t)] \quad . \tag{17}$$

结合式 (15)，式 (16)，可得：

$$\hat{I}(t)=b(t)\cos\varphi(t)+ib(t)\sin\varphi(t) \quad . \tag{18}$$

此时，干涉信号的相位函数$\varphi(t)$可表示为：

$$\varphi(t)=\arctan\left[\frac{\mathrm{Im}(\hat{I}(t))}{\mathrm{Re}(\hat{I}(t))}\right]=\arctan\left[\frac{b(t)\sin\varphi(t)}{b(t)\cos\varphi(t)}\right] \quad . \tag{19}$$

由式 (19) 可得，t_1时刻到t_2时刻，干涉信号$I(t)$的相位变化量$\Delta\varphi$可表示为：

$$\Delta\varphi=\varphi_{\mathrm{u}}(t_2)-\varphi_{\mathrm{u}}(t_1) \quad . \tag{20}$$

需要注意的是，干涉信号的信噪比是影响 HT 相位求解精度的关键因素[16]。干涉信号受测量环境扰动、光电探测器噪声等因素影响，尤其在长距离测量条件下，其信噪比往往较低，故此处利用 EMD 对干涉信号进行自适应分解，并重构出高质量的干涉信号，提高干涉信号相位提取精度。在信号分解方面 EMD 并不依赖于基函数，完全根据信号本身的极值点分布进行自适应分解，将包含多种频率成分的复杂信号逐级分解为多个单频分量之和的形式，适用于具有非平稳特性的复杂信号的分析处理，EMD 分解的具体过程描述如下：

(1) 先提取原始信号$s(t)$的上下极值点，分别用三次样条拟合上下极值点得到上包络信号$e_{\mathrm{u}}(t)$和下包络信号$e_{\mathrm{d}}(t)$。

(2) 求得上下包络的均值包络信号$m(t)$，从初始信号$s(t)$中剔除掉$m(t)$，得到信号$c(t)$。

(3) 将$c(t)$视为新的$s(t)$信号，重复步骤 (1)~(2)，直到最新分解出的$c(t)$满足分解终止条件[17]，此时$c(t)$视为第一阶分量IMF_1。

(4) 从$s(t)$中剔除掉IMF_1，剩余信号记作$r(t)$，将$r(t)$视为新的$s(t)$信号，重复步骤 (1)~(3)，依次得到各阶分量IMF_i。

非平稳信号$s(t)$的分解形式可表示为：

$$s(t)=\sum_{i=1}^{n}IMF_i+r_n(t) \quad , \tag{21}$$

式中，IMF_1，IMF_2，$\cdots$，IMF_n为 EMD 分解所得的各阶分量，也称为本征模态函数 (Intrinsic Modal Function, IMF)，图 3 为 EMD 对实测非平稳干涉信号的分解重构示意图。

在理想情况下，每个 IMF 中仅包含一种特征频率。然而，EMD 在对信号分解的过程中，同一个 IMF 分量中混杂着不同的特征频率，或是不同的 IMF 中存在着相同的特征频率，WU ZH H 和 HUANG N E 等[19] 将这种现象定义为模态混叠。由于模态混叠的存在，导致 EMD 分解得到的相邻两个 IMF 分量之间存在相互干扰，特征频率混杂，无法区分。因此，在对非平稳信号进行分解重构的过程中，不可避免地会剔除掉信号本身的真实分量或是将虚假分量引入到重构信号中，以至于严重影响了信号的重构质量。如图 3 中的IMF_4，一般将该分量视为反映干涉信号特征的最主要的分量。显然，受模态混叠的影响，IMF_4分量中混入了其他频率成分，导致其在时域上产生了一定的波动，因此直接影响了重构干涉信号$I_r(t)$的质量，继而影响了干涉信号的相位提取精度。

为了克服模态混叠问题，YEH J R 等[20] 在 EMD 的基础上提出了 CEEMD 算法。CEEMD 算法先后向原始信号中添加成对 (一正一负) 的白噪声，再分别进行 EMD 分解，算法流程如图 4 所示。CEEMD 算法利用白噪声在时频空间上均匀分布的特性，将不同时频尺度的分量信号IMF_i通过白噪声背景自动映射到与之相关的适当的时频尺度上，以保证每个分量在时域上的连续性进而减少模态混叠。此外，利用白噪声的时域零均值特性，CEEMD 算法通过多次添加白噪声对，并对多组同阶的 IMF 分量取平均，以消除所加白噪声对原始信号的影响。

以下是 CEEMD 算法分解重构的详细过程，先向原始信号$s(t)$中添加成对的白噪声信号$n(t)$，即：

$$\begin{bmatrix} s_{j1}(t) \\ s_{j2}(t) \end{bmatrix} = \begin{bmatrix} 1 & 1 \\ 1 & -1 \end{bmatrix} \begin{bmatrix} s(t) \\ n_j(t) \end{bmatrix} \quad , \tag{22}$$

原始信号$s(t)$第j次添加白噪声对后的合成信号分别为$s_{j1}(t)$和$s_{j2}(t)$，分别对$s_{j1}(t)$和$s_{j2}(t)$进行 EMD 分解，每次分解将得到两组n层IMF分量，即：

$$\begin{bmatrix} s_{j1}(t) \\ s_{j2}(t) \end{bmatrix} = \begin{bmatrix} IMF_{j1,1} & IMF_{j2,1} \\ IMF_{j1,2} & IMF_{j2,2} \\ \vdots & \vdots \\ IMF_{j1,n} & IMF_{j2,n} \\ r_{j1,n}(t) & r_{j2,n}(t) \end{bmatrix}^{\mathrm{T}} \quad . \tag{23}$$

对各层的同阶分量取平均，可得：

$$\boldsymbol{s}_j(t) = \begin{bmatrix} \dfrac{IMF_{j1,1}+IMF_{j2,1}}{1} \\ \dfrac{IMF_{j1,2}+IMF_{j2,2}}{2} \\ \vdots \\ \dfrac{IMF_{j1,n}+IMF_{j2,n}}{2} \end{bmatrix} \quad . \tag{24}$$

当在式 (22)~(24) 中，$j = 1,2,\cdots,m$时，可得到n行m列的分量矩阵，即：

$$\begin{bmatrix} s_1 \\ s_2 \\ \vdots \\ s_j \end{bmatrix} = \begin{bmatrix} IMF_{1,1} & IMF_{2,1} & \cdots & IMF_{j,1} \\ IMF_{1,2} & IMF_{2,2} & \cdots & IMF_{j,2} \\ \vdots & \vdots & \ddots & \vdots \\ IMF_{1,n} & IMF_{2,n} & \cdots & IMF_{j,n} \end{bmatrix}^{\mathrm{T}} \quad . \tag{25}$$

对分量矩阵中的各层同阶分量求平均，可得 CEEMD 分解信号的分量矩阵，即：

$$\boldsymbol{s}(t) = \begin{bmatrix} \dfrac{1}{m}\cdot\sum_{j=1}^{m} IMF_{j,1} \\ \dfrac{1}{m}\cdot\sum_{j=1}^{m} IMF_{j,2} \\ \vdots \\ \dfrac{1}{m}\cdot\sum_{j=1}^{m} IMF_{j,n} \end{bmatrix} = \begin{bmatrix} IMF_1 \\ IMF_2 \\ \vdots \\ IMF_n \end{bmatrix} \quad . \tag{26}$$

图 5 为 CEEMD 算法对实测干涉信号的分解重构示意图，各阶分量按频率从大到小依次排列，通过去除掉高频虚假分量和残余分量，对剩余的真实分量进行重构，得到高信噪比的重构干涉信号$I_{\mathrm{r}}(t)$。

与 EMD 算法分解相比，CEEMD 算法分解出的分量更多，各分量间的特征区分更为清晰，这表明 CEEMD 算法在一定程度上能够降低相邻 IMF 之间的相互干扰。对比图 3 和图 5 中重构干涉信号$I_{\mathrm{r}}(t)$的质量可知，CEEMD 算法对干涉信号的重构质量要优于 EMD 算法，显然，CEEMD 算法将有助于提高干涉信号的相位求解精度。接下来，将通过仿真和实验对 CEEMD 算法的有效性进行验证。

3　实验结果

3.1　FSI 系统实验平台设置

本实验构建的 FSI 测距平台及实验相关设备如图 6 所示，通过上位机对 ECDL(TLB-6712, Newport) 和数据采集卡 (PXIe-5105, National Instruments) 进行控制，设定 ECDL 的调频范围为 765~775 nm，调频速度为 2 nm/s。光纤分路器 (TN785-R3A1, Thorlabs) 将光源分为两路，经准直器 (F230-APC-780, Thorlabs) 耦合到自由空间，其中，25% 的光进入 FP 标准具 (SA200-5B, Thorlabs)，由 FP 标准具内置光电探测器检测 FP 信号，经 FP 控制器将 FP 信号滤波放大；75% 的光进入测量光路，经过迈克尔逊干涉光路后，在 PD(Model 1801, Newport) 处形成干涉，由 PD 将光干涉信号转化为电压信号。DAQ 对 FP 信号和干涉信号进行同步采集，PC 端将对采集到的信号进行处理，完成距离测量。

3.2　FSI 仿真参数设置

为验证算法的有效性，本文对由 F-P 标准具所获得的透射信号的峰值点进行拟合，得到 ECDL 输出的实际光频变化曲线$\upsilon(t)$，此时 ECDL 输出的光频扫描速率β可表示为：

$$\beta(t) = \frac{\mathrm{d}\upsilon(t)}{\mathrm{d}t} \quad , \tag{27}$$

将式 (27) 代入式 (2)，并向仿真干涉信号中添加噪声$n_p(t)$，得到仿真干涉信号的最终形式：

$$I'(t) = a\cdot\cos\left[2\pi(\upsilon_0+\beta(t)\cdot t)\cdot\frac{2n\cdot L}{c}\right] + b\cdot n_p(t) \quad , \tag{28}$$

式中，a 为干涉信号的幅值，b 为噪声信号幅值。仿真参数设置如表 1 所示。

3.3 FSI 仿真实验结果

本节，将以第 2 章的分析为理论依据，对 CEEMD-HT 算法和 EMD-HT 算法的测距性能进行对比验证。首先，对不同信噪比下的干涉信号的单周期相位差进行了 20 次重复提取，并将提取结果与标准的单周期相位差进行比对，以此来反映上述两种算法对小数周期相位的提取能力。如图 7 所示，与直接提取的单周期相位差相比，两种算法均能够降低单周期相位差的提取误差和标准差，同时，不同信噪比条件下，CEEMD-HT 算法对单周期相位差的提取效果均优于 EMD-HT 算法。

接下来，为验证 CEEMD-HT 算法的总体测量性能，先后运用 CEEMD-HT 算法和 EMD-HT 算法对不同信噪比条件下的距离进行了 500 次重复测量，并与仿真设置的标准距离 10 m 进行了对比。如图 8 所示为不同信噪比条件下得到的测量残差与测量标准差的直方图。结果表明，与直接测量相比，CEEMD-HT 算法和 EMD-HT 算法在一定程度上均能够提高 FSI 的测距性能。

值得注意的是，在仿真干涉信号信噪比为 20 dB 时，与直接测量相比，EMD-HT 算法并未表现出明显的测量优势。结合图 3 与 EMD 分解重构原理进一步分析可知，EMD 在对干涉信号进行分解时，需要依赖干涉信号的极值点分布，当仿真干涉信号信噪比相对提高时，其极值点分布的波动性降低，该情况会加剧模态混叠，对 EMD 算法的分解性能产生一定的影响。因而，在进行干涉信号重构时，不但会使部分高频噪声分量混入到重构信号当中，同时也会造成干涉信号真实分量的损失，继而对相位差的提取产生一定的影响，此外，结合第 2 章的分析，在进行相位段划分时，也依赖于干涉信号的极值点分布，因此，重构干涉信号在时域上的平滑程度会对信号段的截取产生相应的影响，继而影响到相位差提取的稳定性，导致该信噪比条件下 EMD 算法测量稳定性的相对下降。

与 EMD 算法相比，CEEMD 在对干涉信号进行分解的过程中，向待分解的干涉信号中加入白噪声对，这使得不同信噪比的干涉信号在时域上的波动程度趋于一致，因此，CEEMD 算法的分解重构性能受信噪比的影响相对较小。由图 8 所示的仿真测距结果可知，在干涉信号信噪比一定的条件下，CEEMD-HT 算法的测量残差和标准差均要低于 EMD-HT 算法和直接测量的结果。值得注意的是，相较于改善系统测量的准确性，CEEMD-HT 算法能够更为有效地提高系统测量的重复性。在干涉信号信噪比为 25 dB 时，10 m 测距范围内，CEEMD-HT 的测量标准差为 3.14 μm。

此外，CEEMD 在对干涉信号进行处理时，需要多次添加噪声及进行多次 EMD 分解，这在一定程度上增加了算法的复杂性，降低了信号处理的效率，而对于测量而言，测量快速性是不容忽视的性能指标。鉴于此，本文对 CEEMD-HT 算法的测量时间和效率进行了评估分析。如图 9 所示，在同一测量条件下，CEEMD-HT 算法的测量效率要低于 EMD-HT 算法和直接测量。

综上所述，CEEMD-HT 算法在提升信号处理性能的同时，其算法简洁性和处理效率也受到了相应的影响，无法同时兼顾系统测量的稳定性和快速性。但是，作为一种自适应信号处理手段，在不增加系统复杂度和成本的基础上，依旧能够提升 FSI 系统的稳定性和抗干扰能力，对改善 FSI 系统的性能具有一定的积极意义。

3.4 实验与结果

FSI 测距实验系统如图 6 所示，设置数据采集装置的采样率为 10 MS/s，单次采样时间为 5 s，并对 FP 信号和干涉信号进行同步采集。在对干涉信号相位段进行划分后，分别运用 CEEMD-HT 算法和 EMD-HT 算法对小数相位段的干涉信号进行分解重构，并对重构信号的相位差进行求解，最后将光频变化范围$\Delta\upsilon$和所截取的干涉信号的相位差$\Delta\varphi$代入测距公式 (7)，进行距离测量。

在进行距离测量之前，对 CEEMD-HT 算法和 EMD-HT 算法处理实测干涉信号的性能进行了对比分析，结果如图 10 所示，图 10(a) 所示为受噪声干扰的实测干涉信号，经 CEEMD 算法和 EMD 算法处理后，得到如图 10(b) 和图 10(c) 所示的重构干涉信号。对比局部放大信号可知，CEEMD 算法和 EMD 算法均能有效降低噪声对干涉信号的干扰。但是，经 EMD 处理后的干涉信号在时域上仍然存在波动，这种波动无论是在进行相位段划分时，还是使用 HT 进行相位求解时均会产生一定的影响。由此可见，相同条件下 CEEMD 算法对干涉信号的处理效果更为明显。

在上述分析的基础上，本节对 CEEMD-HT 算法的实际测量性能进行了实验验证，在 2 m 自由空间范围内对同一目标进行了 50 次重复测量，测距结果如图 11 所示。实验结果表明：在 2 m 自由空间测量范围内，基于 CEEMD-HT 算法的重复测量标准差为 2.79 μm，较 EMD-HT 算法的重复测量标准差 14.48 μm 降低了 5.19 倍，较直接测量重复测量标准差 23.09 μm 降低了 8.28 倍。由此可见，CEEMD-HT 算法能够有效提高 FSI 系统测距的稳定性和系统的抗干扰能力。

4　结　论

本文在分析光频扫描非线性对 FSI 系统测距精度影响的基础上，提出了一种基于 CEEMD-HT 的干涉信号相位求解方法，并对 CEEMD-HT 算法在干涉信号相位求解中的应用可行性进行了理论推导和仿真分析。为验证 CEEMD-HT 算法对非平稳干涉信号相位求解的有效性，采用 FSI 实验系统中的真实输出光频率作为仿真条件，进行了仿真实验。仿真结果表明：无论是单周期相位提取还是整体测量，CEEMD-HT 算法的性能表现均优于直接测量和 EMD-HT 算法的性能；在 10 m 仿真测距范围内，CEEMD-HT 算法的测距标准差为 3.14 μm；同时，对算法的测量效率进行了分析，结果表明：CEEMD-HT 算法在测量效率方面要逊色于直接测量和 EMD-HT 算法，其无法同时兼顾系统的测量稳定性和测量效率。此外，利用 FSI 测距系统进行了实测验证，测量结果表明：在 2 m 自由空间测量范围内，基于 CEEMD-HT 算法的测距标准差为 2.79 μm，相较于 EMD-HT 算法和直接测量法测量标准差分别降低了 5.19 倍和 8.28 倍。因此，CEEMD-HT 算法能够有效降低光频扫描非线性以及噪声对干涉信号相位提取及测距稳定性的影响，提高 FSI 测距系统的抗干扰性和鲁棒性。

References:

[1] LU CH, LIU G D, LIU B G, *et al*.. Absolute distance measurement system with micron-grade measurement uncertainty and 24 m range using frequency scanning interferometry with compensation of environmental vibration[J]. *Optics Express*, 2016, 24(26): 30215-30224.

[2] SHI G, ZHANG F M, QU X H, *et al*.. High-resolution frequency-modulated continuous-wave laser ranging for precision distance metrology applications[J]. *Optical Engineering*, 2014, 53(12): 122402.

[3] SHI G, WANG W, ZHANG F M. Precision improvement of frequency-modulated continuous-wave laser ranging system with two auxiliary interferometers[J]. *Optics Communications*, 2018, 411: 152-157.

[4] WANG ZH Y, LIU ZH G, DENG ZH W, *et al*.. Phase extraction of non-stationary interference signal in frequency scanning interferometry using complex shifted Morlet wavelets[J]. *Optics Communications*, 2018, 420: 26-33.

[5] CHENG X R, LIU J CH, JIA L H, *et al*.. Precision and repeatability improvement in frequency-modulated continuous-wave velocity measurement based on the splitting of beat frequency signals[J]. *Optics Express*, 2021, 29(18): 28582-28596.

[6] DALE J, HUGHES B, LANCASTER A J, *et al*.. Multi-channel absolute distance measurement system with sub ppm-accuracy and 20 m range using frequency scanning interferometry and gas absorption cells[J]. *Optics Express*, 2014, 22(20): 24869-24893.

[7] LIU G D, XU X K, LIU B G, *et al*.. Dispersion compensation method based on focus definition evaluation functions for high-resolution laser frequency scanning interference measurement[J]. *Optics Communications*, 2017, 386: 57-64.

[8] XU X K, LONG K, XU J X, *et al*.. The method of dispersion cancellation based on the forward and reverse tuning of a laser frequency-modulated continuous wave system[J]. *Journal of Infrared and Millimeter Waves*, 2021, 40(2): 243-247.

[9] 王登峰, 姚鑫, 焦仲科, 等. 面向天基引力波探测的时间延迟干涉技术[J]. 中国光学, 2021, 14(2): 275-288.
WANG D F, YAO X, JIAO ZH K, *et al*.. Time-delay interferometry for space-based gravitational wave detection[J]. *Chinese Optics*, 2021, 14(2): 275-288. (in Chinese)

[10] GONG H, LIU ZH G, ZHOU Y L, *et al*.. Mode-hopping suppression of external cavity diode laser by mode matching[J]. *Applied Optics*, 2014, 53(4): 694-701.

[11] DENG ZH W, LIU ZH G, LI B, *et al*.. Precision improvement in frequency-scanning interferometry based on

suppressing nonlinear optical frequency sweeping[J]. *Optical Review*, 2015, 22(5): 724-730.

[12] GONG H, LIU ZH G, ZHOU Y L, *et al*.. Extending the mode-hop-free tuning range of an external-cavity diode laser by synchronous tuning with mode matching[J]. *Applied Optics*, 2014, 53(33): 7878-7884.

[13] YÜKSEL K, WUILPART M, MÉGRET P. Analysis and suppression of nonlinear frequency modulation in an optical frequency-domain reflectometer[J]. *Optics Express*, 2009, 17(7): 5845-5851.

[14] AHN T J, LEE J Y, KIM D Y. Suppression of nonlinear frequency sweep in an optical frequency-domain reflectometer by use of Hilbert transformation[J]. *Applied Optics*, 2005, 44(35): 7630-7634.

[15] ROOS P A, REIBEL R R, BERG T, *et al*.. Ultrabroadband optical chirp linearization for precision metrology applications[J]. *Optics Letters*, 2009, 34(23): 3692-3694.

[16] DENG W, LIU ZH G, DENG ZH W, *et al*.. Extraction of interference phase in frequency-scanning interferometry based on empirical mode decomposition and Hilbert transform[J]. *Applied Optics*, 2018, 57(9): 2299-2305.

[17] BEDROSIAN E. A product theorem for Hilbert transforms[R]. Santa Monica: RAND Corporation, 1962.

[18] RILLING G, FLANDRIN P, GONÇALVES P. On empirical mode decomposition and its algorithms[C]. *Proceedings of IEEE-EURASIP Workshop on Nonlinear Signal and Image Processing NSIP-03*, IEEE, 2003: 8-11.

[19] WU ZH H, HUANG N E. Ensemble empirical mode decomposition: a noise-assisted data analysis method[J]. *Advances in Adaptive Data Analysis*, 2009, 1(1): 1-41.

[20] YEH J R, SHIEH J S, HUANG N E. Complementary ensemble empirical mode decomposition: A novel noise enhanced data analysis method[J]. *Advances in Adaptive Data Analysis*, 2010, 2(2): 135-156.

Author Biographics：

Yang Ke-yuan (1983—), male, born in Jining, Shandong Province, postdoctoral researcher, graduated from University of Electronic Science and Technology in June 2010, mainly engaged in the research on aircraft measurement and control technology, inter-satellite measurement technology. E-mail: ykymail@126.com

杨克元(1983—)，男，山东济宁人，硕士，2010 年 6 月于电子科技大学信号与信息处理专业获得硕士学位，2010 年至今，工作于西安空间无线电技术研究所，从事测控技术、星间测量技术方面的研究。E-mail: ykymail@126.com

Deng Zhong-wen (1987—), male, from Karamay, Xinjiang, lecturer, Ph.D., received his Ph.D. degree from the School of Mechanical Engineering, Xi'an Jiaotong University in 2020, mainly engaged in the research of high-precision large-scale measurement and optical frequency scanning interferometry. E-mail: zwdeng@xidian.edu.cn

邓忠文(1987—)，男，新疆克拉玛依人，讲师，博士，2020 年于西安交通大学机械工程学院获得博士学位，主要从事高精度大尺寸测量，光频扫描干涉测量方面的研究。E-mail: zwdeng@xidian.edu.cn